mathematics

MDPI

Article

PDE-Based Two-Dimensional Radiomagnetotelluric forward Modelling Using Vertex-Centered Finite-Volume Scheme

Wei Xie [1,2], Wendi Zhu [1,2], Xiaozhong Tong [1,2,3,*] and Huiying Ma [4]

[1] School of Geosciences and Info-Physics, Central South University, Changsha 410083, China; xw76676372@csu.edu.cn (W.X.); 8211201304@csu.edu.cn (W.Z.)
[2] Key Laboratory of Non-Ferrous and Geological Hazard Detection, Central South University, Changsha 410083, China
[3] Key Laboratory of Metallogenic Prediction of Nonferrous Metals and Geological Environment Monitoring, Ministry of Education, Central South University, Changsha 410083, China
[4] Hunan Institute of Geological Survey, Changsha 410114, China; csuxw0818@gmail.com
* Correspondence: csumaysnow@csu.edu.cn

Abstract: An efficient finite-volume algorithm, based on the vertex-centered technique, is proposed for solving two-dimensional radiomagnetotelluric forward modeling. Firstly, we derive the discrete expressions of the radiomagnetotelluric Helmholtz-type equation and the corresponding mixed boundary conditions using the vertex-centered finite-volume technique. Then, the corresponding approximate solutions of the radiomagnetotelluric forward problem can be calculated by applying the finite-volume scheme to treat the boundary conditions. Secondly, we apply the finite-volume algorithm to solve two-dimensional Helmholtz equations and the resistivity half-space model. Numerical experiments demonstrate the high accuracy of the proposed approach. Finally, we summarize the radiomagnetotelluric responses through a numerical simulation of a two-dimensional model, which enables qualitative interpretation of field data. Furthermore, our numerical method can be extended and implemented for three-dimensional radiomagnetotelluric forward modeling to achieve more accurate computation.

Keywords: radiomagnetotelluric; forward modelling; finite-volume algorithm; vertex-centered technique; two-dimensional

MSC: 86A25

check for updates

Citation: Xie, W.; Zhu, W.; Tong, X.; Ma, H. PDE-Based Two-Dimensional Radiomagnetotelluric forward Modelling Using Vertex-Centered Finite-Volume Scheme. *Mathematics* **2024**, *12*, 2096. https://doi.org/10.3390/math12132096

Academic Editor: Mariusz Białecki

Received: 18 May 2024
Revised: 30 June 2024
Accepted: 2 July 2024
Published: 3 July 2024

Copyright: © 2024 by the authors. Licensee MDPI, Basel, Switzerland. This article is an open access article distributed under the terms and conditions of the Creative Commons Attribution (CC BY) license (https://creativecommons.org/licenses/by/4.0/).

1. Introduction

The radiomagnetotelluric method is an innovative geophysical exploration technique used to reveal subsurface structures of the Earth. It relies on measuring temporal variations of the magnetic and electrical fields using radio transmitters located at a distance [1]. This method extends the very low frequency method and utilizes all accessible radio transmitters located in the far-field zone within the frequency range of 10–1000 kHz. These measurements enable the correlation of electromagnetic field variations with the conductivity distribution. By measuring the orthogonal electromagnetic fields at the surface, radiomagnetotelluric responses can be obtained. Consequently, the radiomagnetotelluric method has found extensive application in various near-surface studies, including mineral deposit investigations [2,3], groundwater exploration [4,5], geological hazard surveys [6,7], urban applications [8], waste site investigations [9,10], and environmental assessments [11,12].

Numerical modeling approaches can be employed to solve the two-dimensional Helmholtz partial differential equation (PDE) in either the electric or magnetic field for obtaining radiomagnetotelluric responses. Radiomagnetotelluric survey design and data interpretation greatly rely on numerical forward modeling. By employing a distinct scheme

in the governing equation, the finite-difference method (FDM) provides an efficient approximate technique for solving PDEs [13]. Simulating the complex geo-electrical structure and obtaining high-accuracy electric and magnetic field components pose significant challenges [14]. The finite-element method (FEM), as another significant numerical technique, is utilized to solve the forward problem of two-dimensional PDE-based radiomagnetotelluric or magnetotelluric surveys [15–17]. The FEM allows for the incorporation of complex real-world information, such as surface topography, in constructing the initial model, thereby enhancing the flexibility of mesh discretization. However, achieving high accuracy necessitates fine meshing, leading to increased computational costs [18].

The finite-volume method (FVM) can efficiently solve the geophysical forward-modeling problems when formulated as PDEs with appropriate boundary conditions or initial conditions [19]. Over the past few decades, the FVM has gained popularity due to its implementation simplicity and accuracy [20–22]. In theory, the finite-volume approach can combine the mesh flexibility and superior accuracy of the FEM with the straightforward implementation and economical computational load of the finite-difference scheme [23]. In addition, the FVM can be easily applied to solve the nonlinear Helmholtz equation [24,25]. In this work, we present a vertex-centered finite-volume approach for simulating two-dimensional radiomagnetotelluric responses, taking into consideration the presence of displacement currents.

The remainder of this paper is organized as follows. Section 2 derivates the corresponding boundary value problems for the frequency–domain electromagnetic fields. In Section 3, we present the algebraic equations of the vertex-centered finite-volume algorithm for two-dimensional radiomagnetotelluric forward problem. Section 4 presents numerical experiments that validate the accuracy and efficiency of the proposed forward algorithm. Section 5 summarizes the main conclusions of this work.

2. Governing Equations

2.1. Electromagnetic Equations

Maxwell's equations represent the mathematical formulations of the electromagnetic fields, written in the complex–frequency domain as

$$\nabla \times \boldsymbol{E} = -\mathrm{i}\omega\mu\boldsymbol{H} \tag{1}$$

$$\nabla \times \boldsymbol{H} = (\sigma + \mathrm{i}\omega\varepsilon)\boldsymbol{E} \tag{2}$$

$$\nabla \cdot (\varepsilon\boldsymbol{E}) = q \tag{3}$$

$$\nabla \cdot \boldsymbol{H} = 0 \tag{4}$$

where $\nabla = \hat{i}\frac{\partial}{\partial x} + \hat{j}\frac{\partial}{\partial y} + \hat{k}\frac{\partial}{\partial z}$, $\boldsymbol{E}$ represents the frequency–domain electric field, and $\boldsymbol{H}$ denotes the frequency–domain magnetic field. These fields vary with a time-harmonic factor $\mathrm{e}^{\mathrm{i}\omega t}$. The symbol $\mathrm{i} = \sqrt{-1}$ denotes the imaginary unit, ω represents the angular frequency (Hz), σ denotes the conductivity, μ represents the magnetic permeability, ε denotes the medium's dielectric permittivity (F/m) and q represents the charge density ($\mathrm{C/m^3}$). The values of μ and ε are, respectively, expressed as follows:

$$\mu = \mu_r\mu_0 \tag{5}$$

and

$$\varepsilon = \varepsilon_r\varepsilon_0 \tag{6}$$

Here, μ_r represents the relative permeability and ε_r represents the relative electrical permittivity. The magnetic permeability and dielectric permittivity of the medium are equal to corresponding values in free space μ_0 and ε_0, as $\mu_0 = 4\pi \times 10^{-7}\mathrm{H/m}$, and $\varepsilon_0 = 8.85 \times 10^{-12}\mathrm{F/m}$.

In a perfectly two-dimensional conductivity distribution, the electromagnetic fields exhibit two distinct modes: TE mode and TM mode. Assuming the x-axis aligns with the geological strike, as depicted in Figure 1, the TE mode couples the electric field component E_x with the magnetic field components H_y and H_z through the following equations:

$$\frac{\partial H_z}{\partial y} - \frac{\partial H_y}{\partial z} = (\sigma + \mathrm{i}\omega\varepsilon)E_x \tag{7}$$

$$H_y = -\frac{1}{\mathrm{i}\omega\mu}\frac{\partial E_x}{\partial z} \tag{8}$$

$$H_z = \frac{1}{\mathrm{i}\omega\mu}\frac{\partial E_x}{\partial y} \tag{9}$$

while the TM mode couples H_x to E_y and E_z as follows:

$$\frac{\partial E_z}{\partial y} - \frac{\partial E_y}{\partial z} = -i\omega\mu H_x \tag{10}$$

$$E_y = \frac{1}{\sigma + \mathrm{i}\omega\varepsilon}\frac{\partial H_x}{\partial z} \tag{11}$$

$$E_z = -\frac{1}{\sigma + \mathrm{i}\omega\varepsilon}\frac{\partial H_x}{\partial y} \tag{12}$$

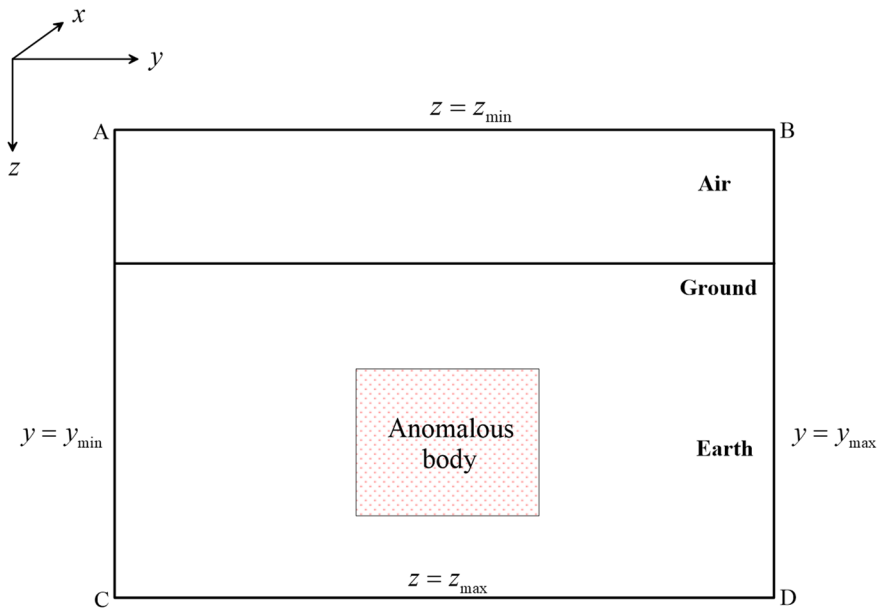


Figure 1. Two-dimensional geo-electrical model of the radiomagnetotelluric problem in the Cartesian coordinate system.

If Equation (7) is associated with Equations (8) and (9), the electric field component E_x of the TE mode satisfies a Helmholtz-type equation:

$$\frac{\partial}{\partial y}\left(\frac{1}{\mathrm{i}\omega\mu}\frac{\partial E_x}{\partial y}\right) + \frac{\partial}{\partial z}\left(\frac{1}{\mathrm{i}\omega\mu}\frac{\partial E_x}{\partial z}\right) - (\sigma + \mathrm{i}\omega\varepsilon)E_x = 0 \tag{13}$$

In the TM mode, the Helmholtz-type equation for the magnetic field component H_x becomes more complex, written as follows:

$$\frac{\partial}{\partial y}\left(\frac{1}{\sigma + \mathrm{i}\omega\varepsilon}\frac{\partial H_x}{\partial y}\right) + \frac{\partial}{\partial z}\left(\frac{1}{\sigma + \mathrm{i}\omega\varepsilon}\frac{\partial H_x}{\partial z}\right) - \mathrm{i}\omega\mu H_x = 0 \tag{14}$$

Consequently, the electromagnetic fields have a general Helmholtz-type equation:

$$\nabla \cdot (\tau \nabla u) + \lambda u = 0 \tag{15}$$

where u, τ, and λ have different interpretations depending on the polarized mode. Specifically, in TE mode:

$$u = E_x, \tau = \frac{1}{\mathrm{i}\omega\mu}, \lambda = -(\sigma + \mathrm{i}\omega\varepsilon) \tag{16}$$

and in TM mode:

$$u = H_x, \tau = \frac{1}{\sigma + \mathrm{i}\omega\varepsilon}, \lambda = -\mathrm{i}\omega\mu \tag{17}$$

2.2. Boundary Conditions

In order to calculate two-dimensional radiomagnetotelluric responses by Equation (15), the corresponding boundary conditions need to be supplied. The computational domain can be confined to a bounded and conductive two-dimensional region, represented by $\Omega = [y_{\min}, y_{\max}] \times [z_{\min}, z_{\max}]$, as depicted in Figure 1. Then, the mixed boundary conditions within the computational domain can be written as

$$u|_{z=z_{\min}} = 1 \text{ (on AB)} \tag{18}$$

$$\left.\frac{\partial u}{\partial y}\right|_{y=y_{\min}} = 0 \text{ (on AC)}, \quad \left.\frac{\partial u}{\partial y}\right|_{y=y_{\max}} = 0 \text{ (on BD)} \tag{19}$$

$$\left.\left(\frac{\partial u}{\partial z} + ku\right)\right|_{z=z_{\max}} = 0 \text{ (on CD)} \tag{20}$$

where $k = \sqrt{-\mathrm{i}\omega\mu\sigma - \mu\varepsilon\omega^2}$, and σ is the conductivity of homogeneous half-space under $z_{\max}$.

3. Finite-Volume Forward Algorithm

To solve the two-dimensional boundary value problem for the radiomagnetotelluric responses, the entire computational domain is discretized into $N \times M$ rectangular cells, as depicted in Figure 2. A rectangular grid with non-uniform and irregular nodes in the y-direction and z-direction is utilized. Discrete nodes in the y-direction are indexed by $i = 1, 2, 3, \cdots, N$, while nodes in the z-direction are indexed by $j = 1, 2, 3, \cdots, M$.

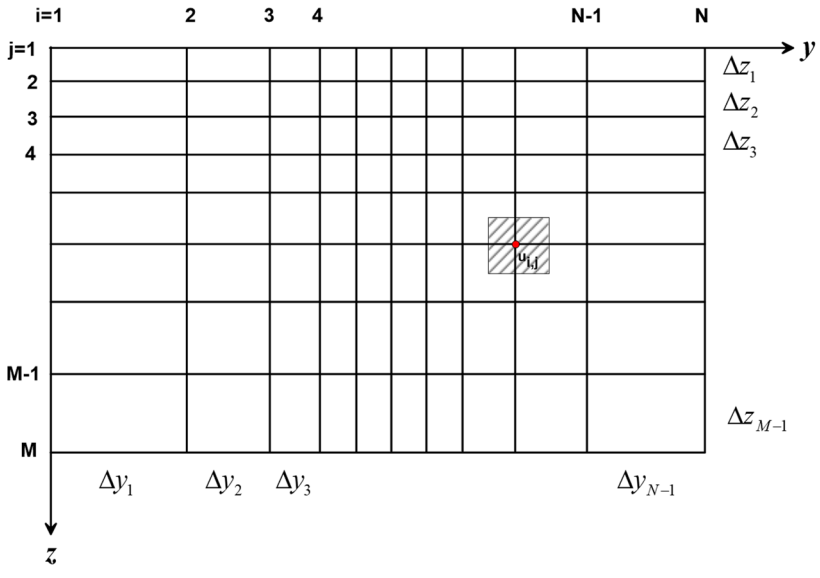


Figure 2. Non-uniform grids for the two-dimensional conductivity model. Red dot represents discrete node.

3.1. Algebraic Equation Form for the Governing Equation

The known conductivity $\sigma(x,z)$ is assigned to each node in y- and z-directions by $\sigma_{i,j}$ using the numerical solution, requiring the evaluation of a discrete set $u_{i,j}$ at each node. For an interior node (i, j), as depicted in Figure 3, the integration of Equation (15) over the control volume yields

$$\iint_{\Delta A_{i,j}} \nabla(\tau \nabla u) \mathrm{d}y\mathrm{d}z + \iint_{\Delta A_{i,j}} \lambda u \mathrm{d}y\mathrm{d}z = 0 \tag{21}$$

Using Green's theorem, Equation (21) is rewritten as follows:

$$\iint_{\Delta A_{i,j}} \nabla(\tau \nabla u) \mathrm{d}x\mathrm{d}z = \oint_{L_{i,j}} \tau \frac{\partial u}{\partial n} \mathrm{d}l \tag{22}$$

where $L_{i,j}$ denotes the enclosed curve of the integral region $\Delta A_{i,j}$ and n represents the outward normal direction.

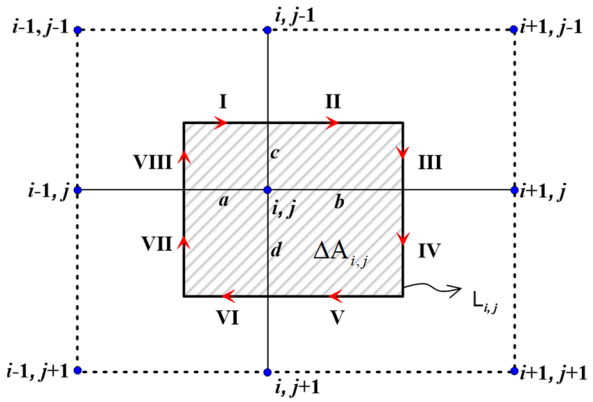


Figure 3. Internal node of the two-dimensional discretized region.

The enclosed curve $L_{i,j}$ consists of eight sections, as depicted in Figure 3. By employing central difference approximating, integrating along the entire path $L_{i,j}$ yields the following algebraic equation:

$$\begin{aligned}\oint_{L_{i,j}} \tau \frac{\partial u}{\partial n} \mathrm{d}l = {} & \frac{\Delta y_{i-1} \cdot \tau_{i-1,j-1}}{2} \left(\frac{u_{i,j-1} - u_{i,j}}{\Delta z_{j-1}} \right) + \frac{\Delta y_i \cdot \tau_{i,j-1}}{2} \left(\frac{u_{i,j-1} - u_{i,j}}{\Delta z_{j-1}} \right) \\ & + \frac{\Delta z_{j-1} \cdot \tau_{i,j-1}}{2} \left(\frac{u_{i+1,j} - u_{i,j}}{\Delta y_i} \right) + \frac{\Delta z_j \cdot \tau_{i,j}}{2} \left(\frac{u_{i+1,j} - u_{i,j}}{\Delta y_i} \right) \\ & + \frac{\Delta y_i \cdot \tau_{i,j}}{2} \left(\frac{u_{i,j+1} - u_{i,j}}{\Delta z_j} \right) + \frac{\Delta y_{i-1} \cdot \tau_{i-1,j}}{2} \left(\frac{u_{i,j+1} - u_{i,j}}{\Delta z_j} \right) \\ & + \frac{\Delta z_j \cdot \tau_{i-1,j}}{2} \left(\frac{u_{i-1,j} - u_{i,j}}{\Delta y_{i-1}} \right) + \frac{\Delta z_{j-1} \cdot \tau_{i-1,j-1}}{2} \left(\frac{u_{i-1,j} - u_{i,j}}{\Delta y_{i-1}} \right)\end{aligned} \tag{23}$$

Similarly, the second integral term of Equation (21) can yield the following algebraic equation:

$$\iint_{\Delta A_{i,j}} \lambda u \mathrm{d}y\mathrm{d}z = \lambda_{i,j} u_{i,j} \left(\frac{\Delta y_{i-1} \cdot \Delta z_{j-1}}{4} + \frac{\Delta y_i \cdot \Delta z_{j-1}}{4} + \frac{\Delta y_i \cdot \Delta z_j}{4} + \frac{\Delta y_{i-1} \cdot \Delta z_j}{4} \right) \tag{24}$$

By substituting the difference approximation of Equations (23) and (24) into Equation (21), the discretized form of the finite-volume scheme is expressed as follows

$$C_W^{ij} u_{i-1,j} + C_E^{ij} u_{i+1,j} + C_N^{ij} u_{i,j-1} + C_S^{ij} u_{i,j+1} + C_P^{ij} u_{i,j} = 0 \tag{25}$$

where C_W^{ij}, C_E^{ij}, C_N^{ij}, C_S^{ij} denote the coupling coefficients, and C_P^{ij} corresponds to the self-coupling coefficient. These coupling coefficients are given by

$$\begin{aligned}
C_W^{ij} &= -\frac{\Delta z_{j-1}\cdot\tau_{i-1,j-1}+\Delta z_j\cdot\tau_{i-1,j}}{2\Delta y_{i-1}},\\
C_E^{ij} &= -\frac{\Delta z_{j-1}\cdot\tau_{i,j-1}+\Delta z_j\cdot\tau_{i,j}}{2\Delta y_i},\\
C_N^{ij} &= -\frac{\Delta y_{i-1}\cdot\tau_{i-1,j-1}+\Delta y_i\cdot\tau_{i,j-1}}{2\Delta z_{j-1}},\\
C_S^{ij} &= -\frac{\Delta y_{i-1}\cdot\tau_{i-1,j}+\Delta y_i\cdot\tau_{i,j}}{2\Delta z_j},\\
C_P^{ij} &= -\left[C_W^{ij}+C_E^{ij}+C_S^{ij}+C_N^{ij}\right]+\lambda_{i,j}\left(\frac{\Delta y_{i-1}\cdot\Delta z_{j-1}}{4}+\frac{\Delta y_i\cdot\Delta z_{j-1}}{4}+\frac{\Delta y_i\cdot\Delta z_j}{4}+\frac{\Delta y_{i-1}\cdot\Delta z_j}{4}\right).
\end{aligned}$$

3.2. Treatment of Mixed Boundary Conditions

3.2.1. Nodes on the Top Edge

The Dirichlet-type boundary conditions are used to the top boundary nodes (i, j) with $i = 1, 2, \cdots, N$ and j = 1, and the corresponding algebraic equation is expressed as follows:

$$u_{i,j} = 1 \tag{26}$$

3.2.2. Nodes on the Bottom Edge

The Robin-type boundary conditions are valid for all boundary nodes (i, j) with $i = 2, 3, \cdots, N-1$ and j = M. The integral region $\Delta A_{i,j}$ is enclosed by the curve $L_{i,j}$ delineated by six sections, as illustrated in Figure 4. By integrating along the entire path $L_{i,j}$, applying central difference approximation yields the following algebraic equation:

$$\begin{aligned}
\oint_{L_{i,j}} \tau\frac{\partial u}{\partial n}\mathrm{d}l = {} & \frac{\Delta y_{i-1}\cdot\tau_{i-1,j-1}}{2}\left(\frac{u_{i,j-1}-u_{i,j}}{\Delta z_{j-1}}\right)+\frac{\Delta y_i\cdot\tau_{i,j-1}}{2}\left(\frac{u_{i,j-1}-u_{i,j}}{\Delta z_{j-1}}\right)\\
& +\frac{\Delta z_{j-1}\cdot\tau_{i,j-1}}{2}\left(\frac{u_{i+1,j}-u_{i,j}}{\Delta y_i}\right)\\
& -\left(\frac{\Delta y_i\cdot\tau_{i,j-1}}{2}+\frac{\Delta y_{i-1}\cdot\tau_{i-1,j-1}}{2}\right)k_{i,j}u_{i,j}\\
& +\frac{\Delta z_{j-1}\cdot\tau_{i-1,j-1}}{2}\left(\frac{u_{i-1,j}-u_{i,j}}{\Delta y_{i-1}}\right)
\end{aligned} \tag{27}$$

Similarly, the second integral term of Equation (21) for the bottom nodes can yield the following algebraic equation:

$$\iint_{\Delta A_{i,j}} \lambda u\mathrm{d}y\mathrm{d}z = \lambda_{i,j}u_{i,j}\left(\frac{\Delta y_{i-1}\cdot\Delta z_{j-1}}{4}+\frac{\Delta y_i\cdot\Delta z_{j-1}}{4}\right) \tag{28}$$

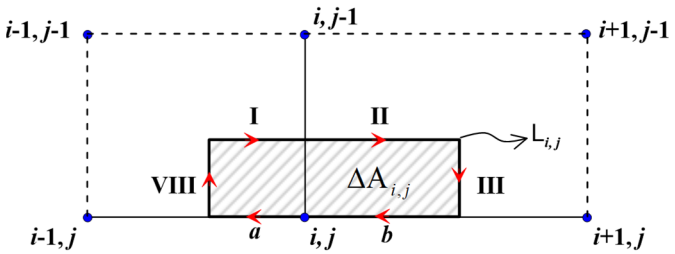


Figure 4. Boundary node on the bottom edge.

By substituting the difference approximation of Equations (27) and (28) into Equation (21), the algebraic equation for any of these nodes is expressed as follows:

$$C_W^{ij}u_{i-1,j}+C_E^{ij}u_{i+1,j}+C_N^{ij}u_{i,j-1}+C_P^{ij}u_{i,j}=0 \tag{29}$$

where the coupling coefficients are given by

$$\begin{aligned}
C_W^{ij} &= -\frac{\Delta z_{j-1}\cdot\tau_{i-1,j-1}}{2\Delta y_{i-1}},\\
C_E^{ij} &= -\frac{\Delta z_{j-1}\cdot\tau_{i,j-1}}{2\Delta y_i},\\
C_N^{ij} &= -\frac{\Delta y_{i-1}\cdot\tau_{i-1,j-1}+\Delta y_i\cdot\tau_{i,j-1}}{2\Delta z_{j-1}},\\
C_P^{ij} &= -\left(C_W^{ij}+C_E^{ij}+C_S^{ij}+C_N^{ij}\right)+\lambda_{i,j}\left(\frac{\Delta y_{i-1}\cdot\Delta z_{j-1}}{4}+\frac{\Delta y_i\cdot\Delta z_{j-1}}{4}\right)\\
&\quad -k_{i,j}\left(\frac{\Delta y_i\cdot\tau_{i,j-1}}{2}+\frac{\Delta y_{i-1}\cdot\tau_{i-1,j-1}}{2}\right).
\end{aligned}$$

3.2.3. Nodes on the Left Edge

The Neumann-type boundary conditions are applied to all boundary nodes (i, j) with $i = 1$ and $j = 2, 3, \cdots, M-1$. The mesh region $\Delta A_{i,j}$ is enclosed by the contour $L_{i,j}$ defined by sections II, III, IV, V, d, c, as shown in Figure 5. By applying the boundary conditions, the finite-volume equation is expressed as follows:

$$C_E^{ij}u_{i+1,j}+C_N^{ij}u_{i,j-1}+C_S^{ij}u_{i,j+1}+C_P^{ij}u_{i,j}=0 \tag{30}$$

where

$$\begin{aligned}
C_E^{ij} &= -\frac{\Delta z_j\cdot\tau_{i,j}+\Delta z_{j-1}\cdot\tau_{i,j-1}}{2\Delta y_i},\\
C_N^{ij} &= -\frac{\Delta y_i\cdot\tau_{i,j-1}}{2\Delta z_{j-1}},\\
C_S^{ij} &= -\frac{\Delta y_i\cdot\tau_{i,j}}{2\Delta z_j},\\
C_P^{ij} &= -\left(C_E^{ij}+C_S^{ij}+C_N^{ij}\right)+\lambda_{i,j}\left(\frac{\Delta y_i\cdot\Delta z_{j-1}}{4}+\frac{\Delta y_i\cdot\Delta z_j}{4}\right).
\end{aligned}$$

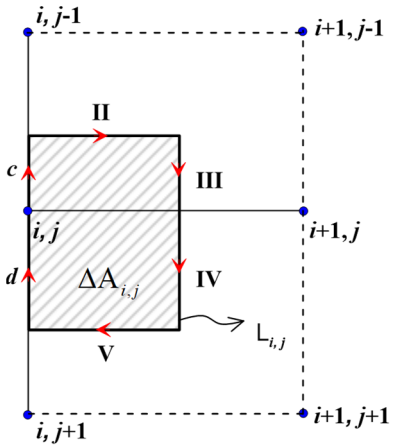


Figure 5. Boundary node on the left edge.

3.2.4. Nodes on the Right Edge

For the nodes (N, j), $j = 2, 3, \cdots, M-1$, the integral region $\Delta A_{i,j}$ is enclosed by the enclosed curve $L_{i,j}$ defined by six sections, as shown in Figure 6. Then, the finite-volume equation is expressed as follows:

$$C_W^{ij}u_{i-1,j}+C_N^{ij}u_{i,j-1}+C_S^{ij}u_{i,j+1}+C_P^{ij}u_{i,j}=0 \tag{31}$$

where

$$\begin{aligned}
C_W^{ij} &= -\frac{\Delta z_j\cdot\tau_{i-1,j}+\Delta z_{j-1}\cdot\tau_{i-1,j-1}}{2\Delta y_{i-1}},\\
C_N^{ij} &= -\frac{\Delta y_{i-1}\cdot\tau_{i-1,j-1}}{2\Delta z_{j-1}},\\
C_S^{ij} &= -\frac{\Delta y_{i-1}\cdot\tau_{i-1,j}}{2\Delta z_j},\\
C_P^{ij} &= -\left(C_W^{ij}+C_S^{ij}+C_N^{ij}\right)+\lambda_{i,j}\left(\frac{\Delta y_{i-1}\cdot\Delta z_{j-1}}{4}+\frac{\Delta y_{i-1}\cdot\Delta z_j}{4}\right).
\end{aligned}$$

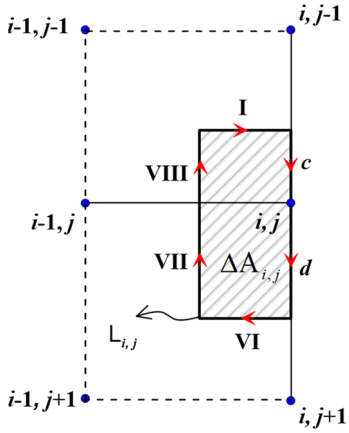


Figure 6. Boundary node on the right edge.

3.2.5. Treatment of Corner Nodes

For the corner nodes (1, M) and (N, M), the corresponding integral region $\Delta A_{i,j}$ is enclosed by the curve $L_{i,j}$ defined by four sections, as shown in Figures 7a and 7b, respectively. In the case of the node (1, M), the finite-volume equation is expressed as follows:

$$C_E^{ij} u_{i+1,j} + C_N^{ij} u_{i,j-1} + C_P^{ij} u_{i,j} = 0 \tag{32}$$

where

$$\begin{aligned} C_E^{ij} &= -\frac{\Delta z_{j-1} \cdot \tau_{i,j-1}}{2\Delta y_i}, \\ C_N^{ij} &= -\frac{\Delta y_i \cdot \tau_{i,j-1}}{2\Delta z_{j-1}}, \\ C_P^{ij} &= -\left(C_E^{ij} + C_N^{ij}\right) + \lambda_{i,j}\left(\frac{\Delta y_i \cdot \Delta z_{j-1}}{4}\right) - k_{i,j}\left(\frac{\Delta y_i \cdot \tau_{i,j-1}}{2}\right). \end{aligned}$$

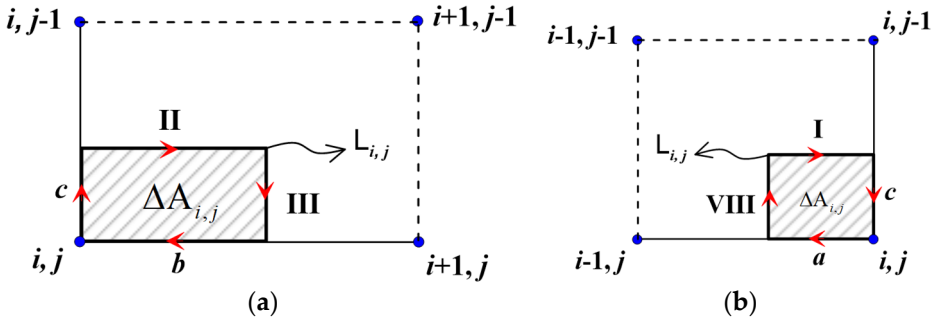


Figure 7. Boundary nodes on the corner on the bottom edge. (**a**) The left corner; (**b**) the right corner.

On the bottom right corner node (N, M), the corresponding algebraic equation is written as follows:

$$C_W^{ij} u_{i-1,j} + C_N^{ij} u_{i,j-1} + C_P^{ij} u_{i,j} = 0 \tag{33}$$

where

$$\begin{aligned} C_W^{ij} &= -\frac{\Delta z_{j-1} \cdot \tau_{i-1,j-1}}{2\Delta y_{i-1}}, \\ C_N^{ij} &= -\frac{\Delta y_{i-1} \cdot \tau_{i-1,j-1}}{2\Delta z_{j-1}}, \\ C_P^{ij} &= -\left(C_W^{ij} + C_N^{ij}\right) + \lambda_{i,j}\left(\frac{\Delta y_{i-1} \cdot \Delta z_{j-1}}{4}\right) - k_{i,j}\left(\frac{\Delta y_{i-1} \cdot \tau_{i-1,j-1}}{2}\right). \end{aligned}$$

3.3. Calculation of Radiomagnetotelluric Responses

After approximating the governing Equation (21) using the finite-volume scheme in all discrete nodes, Equations (25) and (26) and Equations (29)–(33) needed to be appropriately arranged into a linear system, written as follows:

$$\boldsymbol{K}\boldsymbol{u} = \boldsymbol{p} \tag{34}$$

where $\boldsymbol{K}$ represents a sparse matrix, $\boldsymbol{u}$ denotes the unknown vector for either the electric field or the magnetic field at discrete nodes, and $\boldsymbol{p}$ represents the column vector related to the top boundary nodes. Equation (34) can be solved using iterative techniques. Additionally, the convergence speed can be significantly enhanced by applying suitable pre-conditioners. In our computational modeling, combining a bi-conjugate gradient stabilization (BICGSTAB) algorithm [26,27] with an incomplete low-upper (ILU) decomposition [28]. This approach, known as the ILU-BICGSTAB iterative method, is used to solve Equation (34). Figure 8 illustrates the rapid convergence process and total number of iterations for the iterative approach.

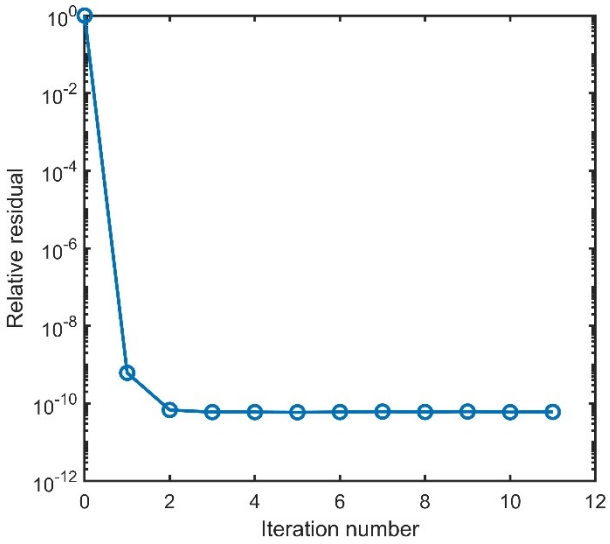


Figure 8. Schematic diagram of the iterative convergence curve.

After obtaining the electric component E_x, the orthogonal magnetic field H_y is solved using Equation (8) in TE mode. Similarly, after acquiring the magnetic field component H_x, the electric component E_y can be solved using Equation (11) in TM mode. Subsequently, the corresponding two-dimensional impedance tensor can be deduced by

$$\begin{bmatrix} E_x \\ E_y \end{bmatrix} = \begin{bmatrix} 0 & Z_{xy} \\ Z_{yx} & 0 \end{bmatrix} \begin{bmatrix} H_x \\ H_y \end{bmatrix} \tag{35}$$

The apparent resistivities can be calculated as

$$\rho_a^{xy} = \frac{1}{\omega\mu}|Z_{xy}|^2,\ \rho_a^{yx} = \frac{1}{\omega\mu}|Z_{yx}|^2 \tag{36}$$

Meanwhile, the impedance phases can be expressed as

$$\phi^{xy} = \arctan\frac{\mathrm{Im}[Z_{xy}]}{\mathrm{Re}[Z_{xy}]},\ \phi^{yx} = \arctan\frac{\mathrm{Im}[Z_{yx}]}{\mathrm{Re}[Z_{yx}]} \tag{37}$$

Based on the analysis of the two-dimensional vertex-centered finite-volume algorithm, the complete workflow, as depicted in Figure 9, enables the computation of approximate radiomagnetotelluric apparent resistivity and impedance phases.

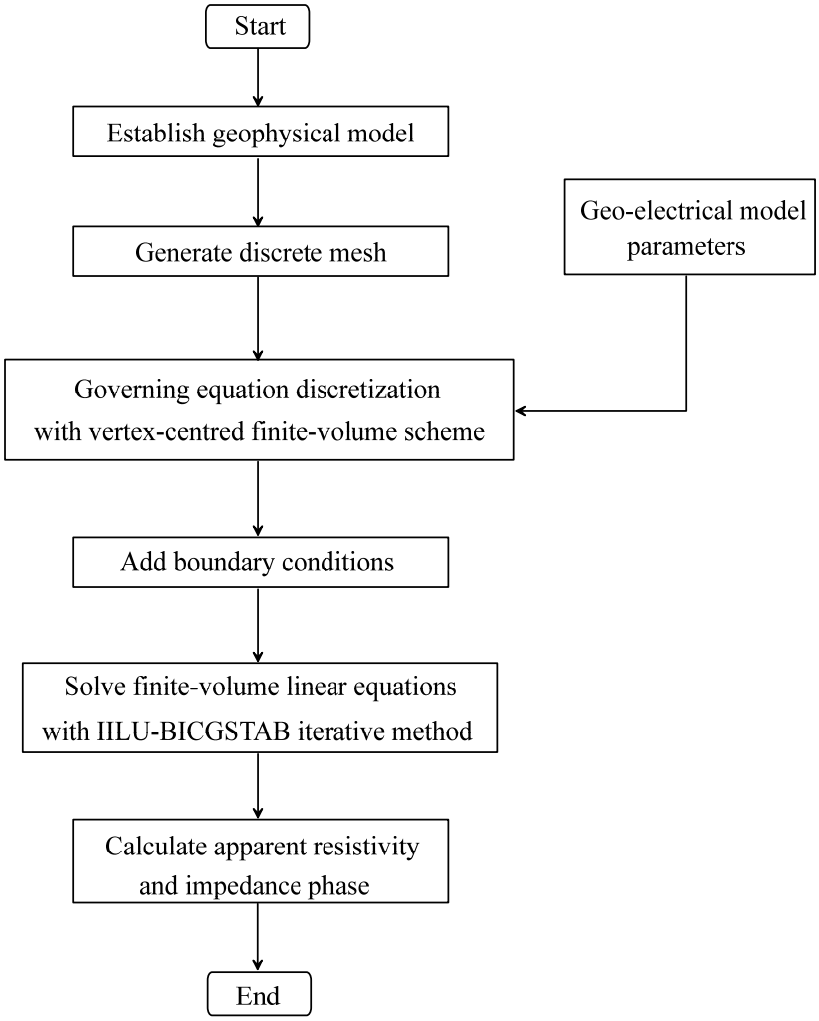


Figure 9. Flow-process diagram of vertex-centered finite-volume forward algorithm.

4. Numerical Experiments and Discussions

Our numerical simulation was executed on the Lenovo Workstation P920, equipped with 2X Gold 6154 processor and 256 GB RAM. The finite-volume forward algorithm was carried out using MATLAB R2023a software (MathWorks Inc., Natick, MA, USA).

4.1. Testing Accuracy with a Helmholtz Equation

We first consider the following Helmholtz equation:

$$\begin{cases} \frac{\partial^2 u}{\partial x^2} + \frac{\partial^2 u}{\partial y^2} + u = \left(1 - 2\pi^2\right) \sin(\pi x) \sin(\pi y), \ \ 0 < x < 2, 0 < y < 4 \\ u|_{x=0} = 0, \ \ u|_{x=2} = 0, \ \ 0 \le y \le 4 \\ u|_{y=0} = 0, \ \ u|_{y=4} = 0, \ \ 0 \le x \le 2 \end{cases}$$

The problem on the computation domain $[0,2] \times [0,4]$ is solved using the vertex-centered finite-volume algorithm and assuming $N = M$. The exact solution of this problem is given by $u(x,y) = \sin(\pi x) \sin(\pi y)$ [29]. In Figure 10, the numerical approximate results and analytical exact results for $N = M = 40$ are presented, demonstrating excellent agreement between numerical approximate solution and analytical exact solution at grid

points (x_i, y_j) (for $i, j = 1, 2, \cdots, 40$). The maximum absolute error is found to be less than 6×10^{-3}.

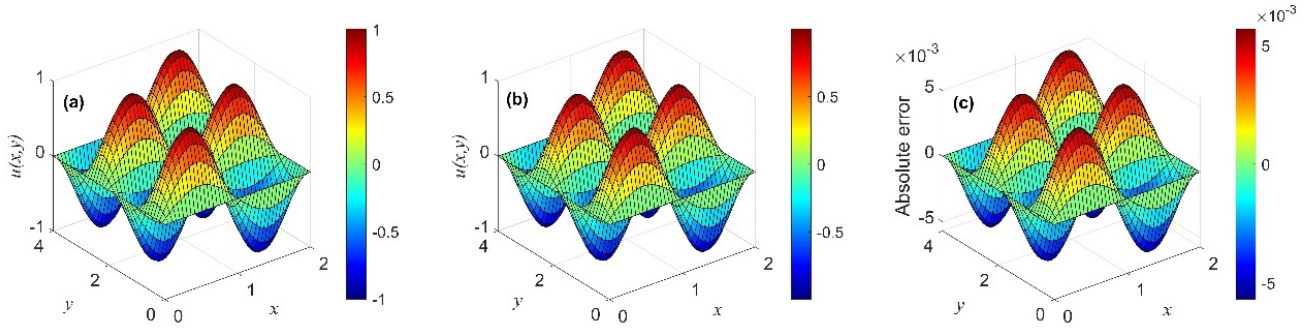


Figure 10. Comparison of numerical and exact solution for the Helmholtz equation. (**a**) Numerical approximate solution; (**b**) analytical exact solution; (**c**) absolute error.

4.2. Testing Efficiency with a Variable-Coefficient Helmholtz Equation

In this experiment, we consider the Helmholtz equation with variable coefficients:

$$\begin{cases} \frac{\partial}{\partial x}\left[A(x,y)\frac{\partial}{\partial x}\right] + \frac{\partial}{\partial y}\left[B(x,y)\frac{\partial}{\partial y}\right] + \lambda u = f(x,y), \ \ 0 < x < \pi, 0 < y < \pi \\ u|_{x=0} = 0, \ \ u|_{x=\pi} = 0, \ \ 0 \le y \le \pi \\ u|_{y=0} = 0, \ \ u|_{y=\pi} = 0, \ \ 0 \le x \le \pi \end{cases}$$

where $\lambda = 1$, $A(x,y) = y$, $B(x,y) = x$, and $f(x,y) = (1 - x - y)\sin(x)\sin(y)$. Homogeneous Dirichlet boundary conditions are imposed on this problem and its exact solution is expressed as $u(x,y) = \sin(x)\sin(y)$.

We point out that the above problem is the one used for measuring the efficiency of numerical methods [29]. In Figure 11, the numerical approximate results and analytical exact results for $N = M = 20$ are presented, demonstrating excellent agreement between numerical approximate solution and analytical exact solution at the grid points (x_i, y_j) (for $i, j = 1, 2, \cdots, 20$). The maximum absolute error is found to be 3.1×10^{-3}.

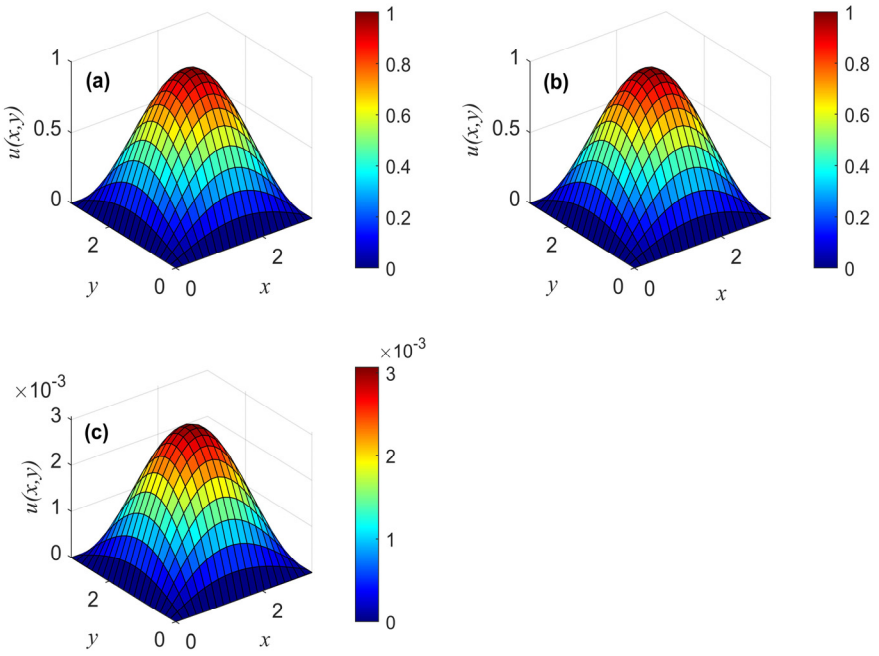


Figure 11. Comparison of numerical and exact solution for the variable-coefficient Helmholtz equation. (**a**) Numerical approximate solution; (**b**) analytical exact solution; (**c**) absolute error.

4.3. Testing Accuracy with a Homogeneous Half-Space Model

A half-space resistivity model [14] is applied for testing the accuracy of the vertex-centered finite-volume forward algorithm for the radiomagnetotelluric problem. The Earth's surface is considered flat, and the homogeneous half-space is characterized by a resistivity of 10,000 $\Omega \cdot$ m and a relative permittivity of $\varepsilon_r = 5$. The radiomagnetotelluric computational domain is set to a size of 10 km $\times$ 10 km, with the air layer extending to a thickness of 10 km.

The vertex-centered finite-volume algorithm was employed to compute finite-volume numerical solutions for the radiomagnetotelluric responses, specifically the apparent resistivities and phases, corresponding to two modes over a frequency range of 10 kHz to 250 kHz, as depicted in Figure 12. It is evident that the numerical radiomagnetotelluric responses obtained using this algorithm exhibit excellent agreement with the analytical exact solutions provided in Appendix A.

The maximum absolute errors for the apparent resistivities and phases in TE mode are 11.55 $\Omega \cdot$ m and 0.028°, respectively. At higher frequencies, the presence of displacement currents leads to a reduction in the apparent resistivity and phase below the commonly observed values of 10,000 and 45°, respectively, as anticipated within the quasi-static approximation.

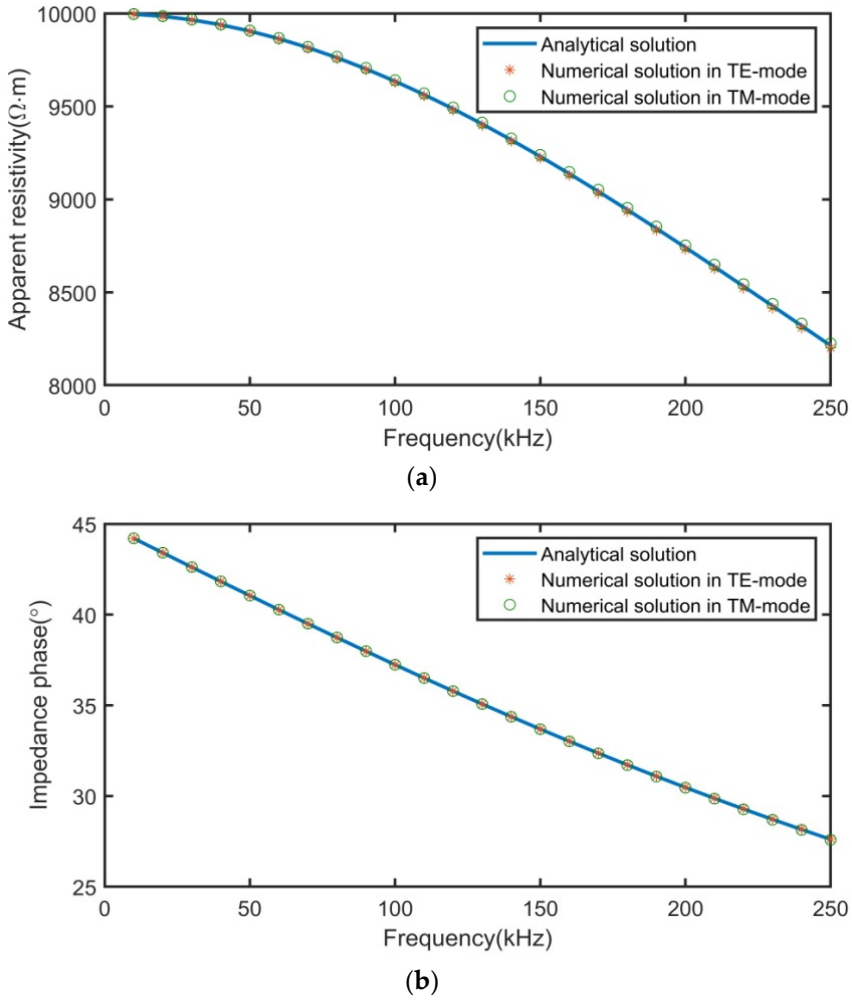


Figure 12. Comparison of the analytical solution and numerical solution of radiomagnetotelluric responses. (**a**) Apparent resistivity; (**b**) impedance phase.

4.4. Testing Accuracy with a Two-Dimensional Geo-Electric Model

To verify the accuracy of the vertex-centered finite-volume algorithm, a two-dimensional geo-electric model [30] is used, as shown in Figure 13. The model consists of two conductive rectangular bodies embedded in a two-layer model. The finite-volume calculations are again compared with the results of the finite-element method by Wannamaker et al. [31].

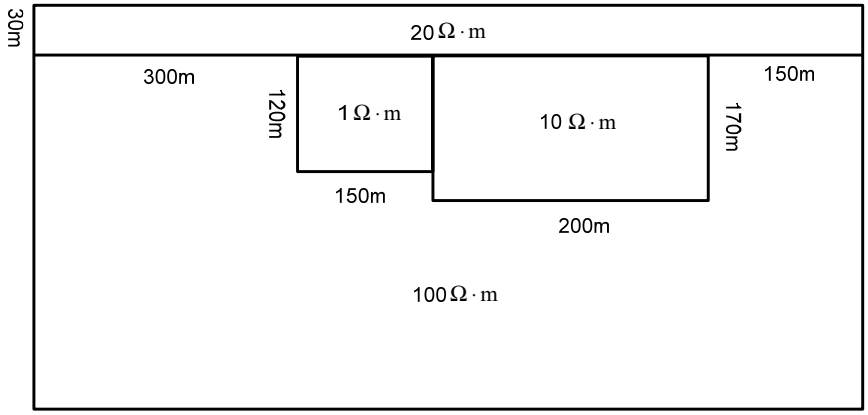


Figure 13. The two-dimensional resistivity model given by Wittke and Tezkan [30].

In this study, the non-uniform meshes in TM mode and TE mode are set as 100 × 80 (in which 10 km is the air media and its resistivity is equal to 10^{15} Ω · m). The measurement profile along the atmospheric grounding interface varies from 0 to 800 m. The frequency to be tested is only 1 kHz. Figures 14 and 15 display the comparison of the finite-element results from Wannamaker et al. (1986) [31] and our finite-volume forward code, and the results match well. The maximum relative apparent resistivity error between the two forward schemes is equal to 0.02% in TM mode and 0.01% in TE mode, respectively. The maximum relative phase error is equal to 0.004% in TM mode and 0.005% in TE mode, respectively.

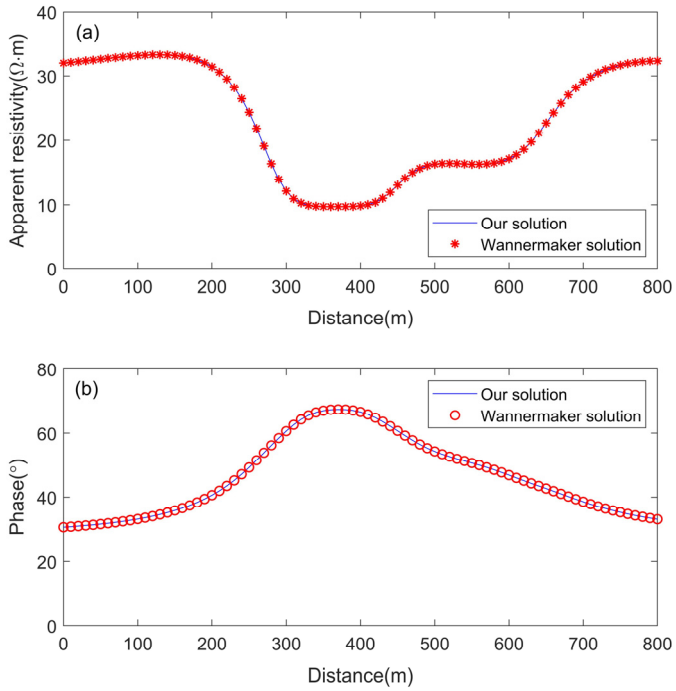


Figure 14. Calculation and comparison for the geo-electric model for frequency f = 1 kHz, TE mode. (**a**) Apparent resistivity; (**b**) impedance phase.

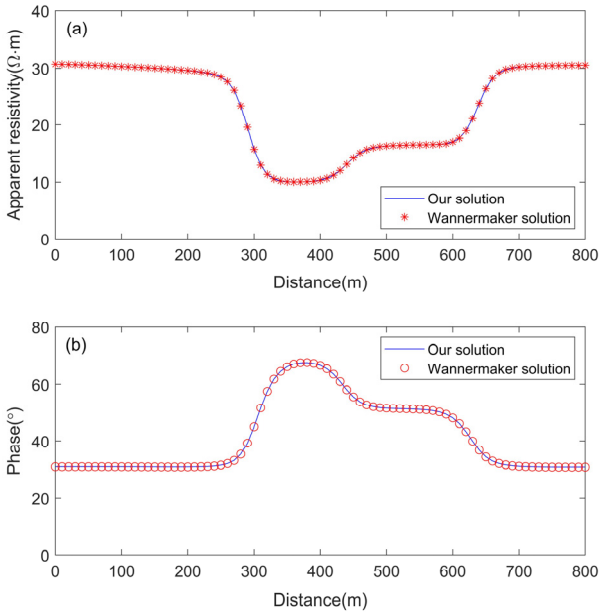


Figure 15. Calculation and comparison for the geo-electric model for frequency f = 1 kHz, TM mode. (**a**) Apparent resistivity; (**b**) impedance phase.

4.5. Single Rectangular Anomaly Example

To demonstrate the efficiency of the vertex-centered finite-volume algorithm, a numerical example was conducted using a simple two-dimensional resistivity anomaly, as depicted in Figure 16. The model consists of a single rectangular block with an embedded resistivity of 1000 $\Omega \cdot$ m. The two-dimensional model's background resistivity is set to 10,000 $\Omega \cdot$ m, while the relative permittivity is $\varepsilon_r = 5$. The resistivity anomaly block has a width of 100 m, a thickness of 45 m, and is positioned at a depth of 15 m from the ground.

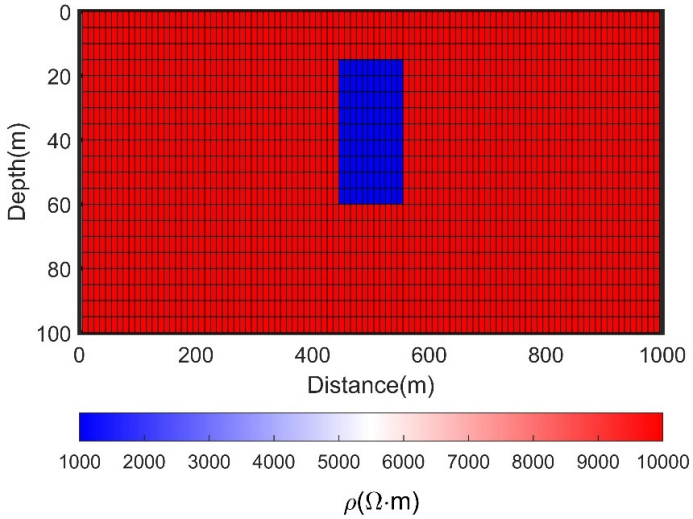


Figure 16. Simple two-dimensional resistivity model.

The whole domain was set to a size of 20 km $\times$ 20 km. A total of nine frequencies of 10, 40, 70, 100, 130, 160, 190, 220, and 250 kHz was selected to evaluate radiomagnetotelluric responses. The calculated apparent resistivities and impedance phases using the finite-volume approach are presented in Figure 17, effectively capturing the geo-electrical parameters of the simple two-dimensional model.

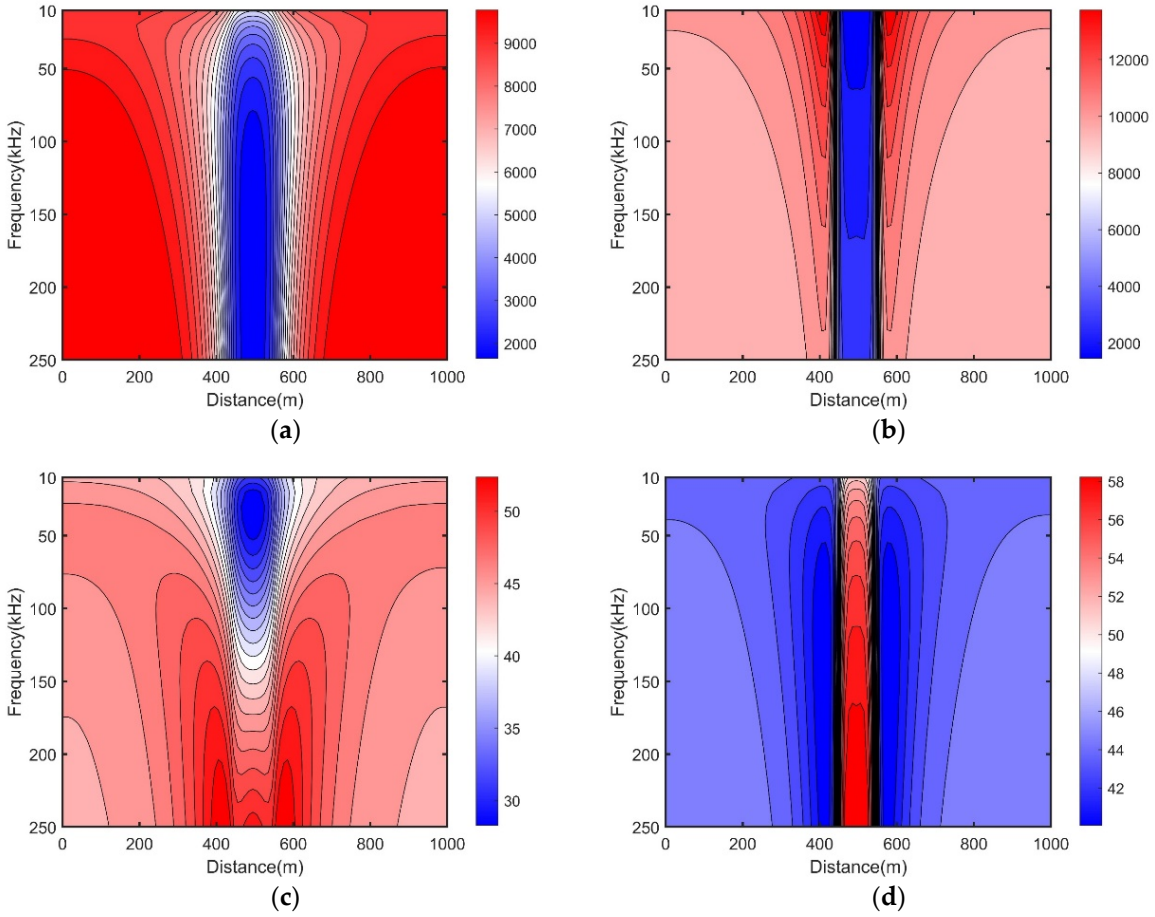


Figure 17. Radiomagnetotelluric approximate responses for the two-dimensional model. (**a**) TE apparent resistivity; (**b**) TM apparent resistivity; (**c**) TE phase; (**d**) TM phase.

5. Conclusions

We have developed an efficient vertex-centered finite-volume algorithm for two-dimensional radiomagnetotelluric forward modeling. Detailed mathematical formulas for the finite-volume approach are presented, and the numerical approach is carried out using MATLAB R2023a software. Numerical examples demonstrate the high accuracy of the proposed algorithm for two-dimensional radiomagnetotelluric forward modeling, enabling qualitative interpretation of field data. Thus, our finite-volume method offers an alternative numerical technique to calculate radiomagnetotelluric responses in the case of two-dimensional earth resistivity models. Furthermore, the vertex-centered finite-volume algorithm can be readily extended and implemented for simulating three-dimensional radiomagnetotelluric responses.

Author Contributions: Conceptualization, W.X. and H.M.; formal analysis, W.Z.; funding acquisition, X.T.; methodology, W.X. and X.T.; project administration, X.T.; visualization, H.M.; supervision, X.T.; writing—original draft preparation, W.X. and W.Z.; writing—review and editing, X.T. and H.M. All authors have read and agreed to the published version of the manuscript.

Funding: This research work was partly supported by the National Natural Science Foundation of China (grant Nos. 42274083 and 41974049) and partly by the Hunan National Natural Science Foundation (grant Nos. 2023JJ30659, 2024JJ8318 and 2022JJ30706).

Data Availability Statement: Data associated with this research are available and can be obtained by contacting the corresponding author.

Acknowledgments: The authors would like to thank Ya Sun, who modified this manuscript for improving English writing quality and gave helpful discussions about the results of models. We

would also like to thank the editors and the reviewers for providing comments that substantially improved the paper.

Conflicts of Interest: The authors declare no conflicts of interest.

Appendix A. Mathematical Expressions for Computing One-Dimensional Radiomagnetotelluric Responses

In a layered one-dimensional model, we calculate the apparent impedance Z_m in the mth layer as follows:

$$Z_m = Z_{0m}\frac{Z_{0m}(1-e^{-2k_m h_m}) + Z_{m+1}(1+e^{-2k_m h_m})}{Z_{0m}(1+e^{-2k_m h_m}) + Z_{m+1}(1-e^{-2k_m h_m})} \tag{A1}$$

where $k_m = \sqrt{-i\omega\mu\sigma_m - \mu\varepsilon_m\omega^2}$, $Z_{0m} = -\frac{i\omega\mu}{k_m}$, and h_m represent the mth layer thickness. Then, the radiomagnetotelluric apparent resistivity and phase can be calculated as

$$\rho_a = \frac{1}{\omega\mu}|Z_1|^2, \varphi = \arctan\frac{\mathrm{Im}[Z_1]}{\mathrm{Re}[Z_1]} \tag{A2}$$

References

1. Tezkan, B.A. Review of environmental applications of quasi-Stationary electromagnetic techniques. *Surv. Geophys.* **1999**, *20*, 279–308. [CrossRef]
2. Bastani, M.; Malehmir, A.; Ismail, N.; Pedersen, L.B.; Hedjazi, F. Delineating hydrothermal stockwork copper deposits using controlled-source and radio-magnetotelluric methods: A case study from northeast Iran. *Geophysics* **2009**, *74*, 167–181. [CrossRef]
3. Malehmir, A.; Wang, S.; Lamminen, J.; Brodic, B.; Bastani, M.; Vaittinen, K.; Juhlin, C.; Place, J. Delineating structures controlling sandstone-hosted base-metal deposits using high-resolution multicomponent seismic and radio-magnetotelluric methods: A case study from Northern Sweden. *Geophys. Prospect.* **2015**, *63*, 774–797. [CrossRef]
4. Pedersen, L.B.; Bastani, M.; Dynesius, L. Groundwater exploration using combined controlled-source and radiomagnetotelluric techniques. *Geophysics* **2005**, *70*, 8–15. [CrossRef]
5. Yogeshwar, P.; Tezkan, B.; Israil, M.; Candansayar, M. Groundwater contamination in the Roorkee area, India: Two-dimensional joint inversion of radiomagnetotelluric and direct current resistivity data. *J. Appl. Geophys.* **2012**, *76*, 127–135. [CrossRef]
6. Wang, S.; Malehmir, A.; Bastani, M. Geophysical characterization of areas prone to quicky-clay landslides using radio-magnetotelluric and seismic methods. *Tectonphysics* **2016**, *677*, 248–260. [CrossRef]
7. Shan, C.; Bastani, M.; Malehmir, A.; Persson, L.; Lundberg, E. Integration of controlled-source and radio magnetotellurics, electric resistivity tomography, and reflection seismics to delineate 3D structures of a quick-clay landslide site in southwest of Sweden. *Geophysics* **2016**, *81*, 13–29. [CrossRef]
8. Bastani, M.; Wang, S.; Malehmir, A.; Mehta, S. Radio-magnetotelluric and controlled-source magnetotelluric surveys on a frozen lake: Opportunities for urban applications in Nordic countries. *Near Surf. Geophys.* **2022**, *20*, 30–45. [CrossRef]
9. Newman, G.A.; Recher, S.; Tezkan, B.; Neubauer, F.M. 3D inversion of a scalar radio magnetotelluric field data set. *Geophysics* **2003**, *68*, 791–802. [CrossRef]
10. Candansayar, M.E.; Tezkan, B. A comparison of different radiomagnetotelluric data inversion methods for buried waste sites. *J. Appl. Geophys.* **2006**, *58*, 218–231. [CrossRef]
11. Turberg, P.; Müller, I.; Flury, F. Hydrogeological investigation of porous environments by radio magnetotelluric-resistivity (RMT-R 12-240 kHz). *J. Appl. Geophys.* **1994**, *31*, 133–143. [CrossRef]
12. Shan, C.; Kalscheuer, T.; Pedersen, L.B.; Erlstrom, M.; Persson, L. Portable audio magnetotellurics—Experimental measurements and joint inversion with radiomagnetotelluric data from Gotland, Sweden. *J. Appl. Geophys.* **2017**, *143*, 9–22. [CrossRef]
13. Tong, X.; Sun, Y. Fictitious point technique based on finite-difference method for 2.5D direct-current resistivity forward problem. *Mathematics* **2024**, *12*, 269. [CrossRef]
14. Kalscheuer, T.; Pedersen, L.B.; Siripunvaraporn, W. Radiomagnetotelluric two-dimensional forward and inverse modelling accounting for displacement currents. *Geophys. J. Int.* **2008**, *175*, 486–514. [CrossRef]
15. Yi, K.; Zhang, Z.; Li, M.; Yuan, Y.; Guo, Y.; Zhou, F. Joint inversion of resistivity and permittivity for two dimensional RMT data based on FCM clustering. *Chin. J. Geophys.* **2022**, *65*, 2340–2350. [CrossRef]
16. Yao, H.; Ren, Z.; Chen, H.; Tang, J.; Li, Y. Two-dimensional magnetotelluric finite element modeling by a hybrid Helmholtz-curl formulae system. *J. Comput. Phys.* **2021**, *443*, 110533. [CrossRef]
17. Sarakorn, W. 2-D magnetotelluric modelling using finite element method incorporating unstructured quadrilateral elements. *J. Appl. Geophys.* **2017**, *139*, 16–24. [CrossRef]
18. Yuan, Y.; Tang, J.; Ren, Z. Two-dimensional complicated radio-magnetotelluric finite-element modeling using unstructured grids. *Chin. J. Geophys.* **2015**, *58*, 4685–4695. [CrossRef]

19. Du, H.; Ren, Z.; Tang, J. A finite-volume approach for two-dimensional magnetotellurics modelling with arbitrary topographies. *Stud. Geophys. Geod.* **2016**, *60*, 332–347. [CrossRef]
20. Jahadari, H.; Farquharson, C.G. A finite-volume solution to the geophysical electromagnetic forward problem using unstructured grids. *Geophysics* **2014**, *79*, 287–302. [CrossRef]
21. Wang, N.; Tang, J.; Ren, Z.; Xiao, X.; Huang, X. Two-dimensional magnetotelluric anisotropic forward modeling using finite-volume method. *Chin. J. Geophys.* **2019**, *62*, 3912–3922. [CrossRef]
22. Guo, Z.; Egbert, G.; Dong, H.; Wei, W. Modular finite volume approach for 3D magnetotelluric modeling of the Earth medium with general anisotropy. *Phys. Earth Planet. Inter.* **2020**, *309*, 106585. [CrossRef]
23. Jahandari, H.; Ansari, S.; Farquharson, C.G. Comparison between staggered grid finite–volume and edge–based finite–element modelling of geophysical electromagnetic data on unstructured grids. *J. Appl. Geophys.* **2017**, *138*, 185–197. [CrossRef]
24. Baruch, G.; Fibich, G.; Tsynkov, S. High-order numerical solution of the nonlinear Helmholtz equation with axial symmetry. *J. Comput. Appl. Math.* **2007**, *204*, 477–492. [CrossRef]
25. Baruch, G.; Fibich, G.; Tsynkov, S. High-order numerical method for the nonlinear Helmholtz equation with material discontinuities in one space dimension. *J. Comput. Phys.* **2007**, *227*, 820–850. [CrossRef]
26. Liu, J.; Liu, P.; Tong, X. Three-dimensional land FD-CSEM forward modeling using edge finite-element method. *J. Cent. South Univ.* **2018**, *25*, 131–140. [CrossRef]
27. Tong, X.; Sun, Y.; Huang, J.; Liu, J. High-accuracy gravity field and gravity gradient forward modelling based on 3D vertex-centered finite-element algorithm. *J. Cent. South Univ.* **2024**, *31*, 1659–1670. [CrossRef]
28. Pan, K.; Wang, J.; Hu, S.; Ren, Z.; Cui, T.; Guo, R.; Tang, J. An efficient cascadic multigrid solver for 3-D magnetotelluric forward modelling problems using potentials. *Geophys. J. Int.* **2022**, *230*, 1834–1851. [CrossRef]
29. Wu, T. A dispersion minimizing compact finite difference scheme for the 2D Helmholtz equation. *J. Comput. Appl. Math.* **2017**, *75*, 497–512. [CrossRef]
30. Wittke, J.; Tezkan, B. Meshfree magnetotelluric modeling. *Geophys. J. Int.* **2014**, *198*, 1255–1268. [CrossRef]
31. Wannamaker, P.E.; Stodt, J.A.; Rijo, L. Two-dimensional topographic responses in magnetotellurics modeled using finite elements. *Geophysics* **1986**, *51*, 2131–2144. [CrossRef]

Disclaimer/Publisher's Note: The statements, opinions and data contained in all publications are solely those of the individual author(s) and contributor(s) and not of MDPI and/or the editor(s). MDPI and/or the editor(s) disclaim responsibility for any injury to people or property resulting from any ideas, methods, instructions or products referred to in the content.